Efficient Electrocatalysts for OER: Amorphous Cerium-Doped Cobalt Sulfide with Enhanced Performance and Durability

Sina Maghool[a], Ali Akbar Asgharinezhad*[,b], Afsanehsadat Larimi*[,c], Cyrus Ghotbi[a], Farhad Khorasheh[a]

[a] Department of Chemical and Petroleum Engineering, Sharif University of Technology, Tehran, Iran

[b] Chemistry and Process Research Department, Niroo Research Institute, Tehran, Iran

[c] School of Engineering and Applied Sciences, Department of Chemical Engineering, Swansea University, Wales, UK

*Corresponding authors' Email: aasgharinezhad@nri.ac.ir (A. A. Asgharinezhad);

a.larimi@swansea.ac.uk (A. Larimi)

Abstract

Developing highly efficient electrocatalysts is essential for advancing the oxygen evolution reaction (OER), a key step in water splitting. In this study, a novel approach for the synthesis of an amorphous sulfide structure has been presented. First, a cerium-doped zeolitic imidazolate framework-67 (Ce-ZIF-67) using a co-precipitation method, followed by a multi-step transformation process. This process includes oxidation to form cerium-doped cobalt oxide (Ce-CO) and a subsequent sulfidation step to produce an amorphous cerium-doped cobalt sulfide (Ce-CS) structure. The introduction of cerium and the formation of an amorphous sulfide structure result in a significantly enhanced OER performance due to increased atomic disorder, improved electron mobility, and an expanded active surface area. Remarkably, the Ce-CS structure achieved a reduction in overpotential from 352 mV for Ce-CO to 291 mV at 100 mA cm^{-2} in 1.0 M KOH, alongside a Tafel slope reduction from 86.2 mA decade^{-1} to 67.2 mV decade^{-1}. These enhancements underline the importance of cerium doping and amorphization in optimizing electrocatalytic efficiency. Furthermore, the Ce-CS catalyst demonstrated exceptional durability, with no observable degradation in performance or structural integrity after 10 h of continuous operation. This work presents a pioneering strategy for designing and synthesizing highly effective OER electrocatalysts, contributing a significant advancement to the field.

Keywords: Oxygen evolution reaction, Amorphous structure, Transition metal oxides, Transition metal oxides.

1. Introduction

The anodic oxygen evolution reaction (OER) is essential for numerous clean energy applications [1,2]. However, the effectiveness of OER is hindered by the slow kinetics resulting from the four-electron/proton transfer mechanisms, which restricts its potential for commercial use [3–5]. There have been reports indicating that noble metal compounds, such as RuO_2 and IrO_2, exhibit excellent catalytic behavior in the OER process [6,7]. However, the high cost and limited availability of noble metals significantly restrict their widespread application [8–10].

Consequently, there significant efforts have been to investigate economically viable and readily available alternatives for the OER, such as transition metal phosphides, sulfides, selenides, and oxides [11,12]. Among these materials, transition metal oxides have undergone thorough investigation and have emerged as promising electrocatalysts for the OER due to their multiple valence states and accessibility [13,14]. In a study by Paul et al. [15], it was demonstrated that oxidized structures exhibit good performance in the OER process. For instance, the Co_3O_4 structure showed an overpotential of 296 mV at a current density of 10 mA cm^{-2}. On the other hand, transition metal sulfide compounds, known for their distinctive structure and tunable electrical properties, are considered promising electrocatalysts for electrochemical reactions [16,17]. In addition, sulfur has a lower electronegativity than oxygen, which improves the movement of electrons in the electrocatalyst, thereby enhancing the efficiency of the electrocatalyst in the OER [18].

Moreover, Metal-organic frameworks (MOFs) are porous structures that are composed of organic ligands and metal ions [19–21]. They serve as highly effective designs for synthesizing compounds containing different metals [22,23]. Moreover, Materials that are cobalt-based have shown remarkable electrocatalytic activity in OER [24], and the zeolitic imidazolate framework-67 (ZIF-

67) with a central ion of cobalt, containing a significant number of active sites, can serve as an effective template for synthesizing cobalt sulfide [25]. This material offers abundant internal space and facilitates quick mass transfer [26]. Additionally, the wet chemical synthesis technique employed in the formation of this structure is acknowledged as a promising strategy for the large-scale fabrication of composites [27]. This industry-suitable method, operating at room temperature and allowing for both thermodynamic and dynamic control, enhances catalyst morphology, increasing active site numbers and improving electrocatalytic performance, making it ideal for practical electrocatalyst applications [28].

Several methods have been implemented for modify the electronic states of compounds, and introducing additional transition metal elements has proven to be an effective approach to enhancing their electrochemical activity [29,30]. Cerium (Ce) is a valuable rare earth element that exhibits a combination of electrical and ionic conductivity due variation between Ce^{3+} and Ce^{4+}, making it an excellent dopant to enhance catalytic activity [31–33]. Furthermore, the robust electrical interaction between Ce and other metal compounds can influence the binding strength of oxygen intermediates on metal centers, thereby enhancing the kinetics of the reaction [34]. Li et al. [35] reported CeO_2−CoO nanofibers with an overpotential of 296 mV at current density of 10 mA cm^{-2}. They demonstrated that the unique arrangement of atoms at the interface between Ce and Co leads to the formation of several oxygen vacancies due to the improper alignment of atomic positions between the two materials, which is helpful for the OER.

In addition to composition, there has been significant research on optimizing the electrochemical activity by improving the availability of active sites and modifying the structure [36]. Amorphous materials have garnered significant interest due to their ability to enhance catalytic performance, attributed to numerous structural defects and increased contact with active sites [37,38]. For

4

example, Huang et al. [39] reported amorphous-CoMoP$_x$/carbon fiber as an amorphous compound with an overpotential of 305 mV at current density of 10 mA cm^{-2}. This study demonstrated that amorphous shapes augment the capacity for mass transfer and fully expose all atoms, hence amplifying the surface area that is electrochemically active.

In light of the aforementioned considerations, this study presents a novel approach by synergistically combining the advantages of cerium doping and the formation of amorphous structures to enhance the OER performance. Specifically, cerium was first doped into the zeolitic imidazolate framework-67 (ZIF-67) framework, which significantly improved the electrochemical activity due to the unique properties of cerium, such as its mixed valence states and robust electronic interactions. Following this, the oxidation of cerium-doped zeolitic imidazolate framework-67 (Ce-ZIF-67) resulted in a crystalline cerium-doped cobalt oxide (Ce-CO) structure, which further increased the active surface area and electron transfer efficiency. Finally, a sulfidation process was employed to convert the crystalline structure into an amorphous cerium-doped cobalt sulfide (Ce-CS) phase, which exhibited superior performance due to the introduction of sulfur and the amorphous nature that facilitates faster electron transfer and lowers overpotential. This comprehensive approach not only highlights the potential of cerium-doped amorphous structures in OER but also offers a scalable and efficient strategy for the development of advanced electrocatalysts, addressing key challenges in the field.

2. Experimental

2.1. Materials

Cerium(III) nitrate hexahydrate (Ce(NO$_3$)$_3$.6H$_2$O), cobalt(II) nitrate hexahydrate (Co(NO$_3$)$_2$.6H$_2$O), 2-methylimidazole (C$_4$H$_6$N$_2$), thiourea (CH$_4$N$_2$S), ethylene glycol (C$_2$H$_6$O$_2$),

carbon black (C), *N*-methyl-2-pyrrolidone (C_5H_9NO), potassium hydroxide (KOH), ethanol (C_2H_6O), acetone (C_3H_6O), and hydrochloric acid (HCl) were obtained from Merck (Darmstadt, Germany). High purity (99%) methanol (CH_3OH) was purchased from Neutron Pharmacochemical Co (Tehran, Iran). Polyvinylidene fluoride ($-(C_2H_2F_2)_n-$) was purchased from Alfa Chemistry (New York, United States). Nickel foam (NF, thickness:0.3 mm) was obtained from American Elements (California, United States). All materials were utilized in their original form with no purifying process.

2.2. Synthesis of ZIF-67 and Ce-ZIF-67

The materials were synthesized using the method depicted in Scheme 1. The synthesis of the ZIF-67 structure was carried out via a coprecipitation process. In beaker number one, 3.9 mmol of $Co(NO_3)_2.6H_2O$ was added to 30 ml of methanol and dissolved. In beaker number two, 15.9 mmol of 2-methylimidazole was dissolved in 30 ml of methanol, yielding a homogeneous solution. Subsequently, the homogeneous solution from beaker number two was gently added to beaker number one. The precipitate was washed three times with pure methanol, then placed in an oven at 60 °C for 12 h to obtain the ZIF-67 structure.

Moreover, the synthesis of Ce-ZIF-67 was conducted using a similar procedure, with the exception that during the initial phase of synthesis, 0.2 mmol of $Ce(NO_3)_3.6H_2O$ were added to the solution in addition to 3.7 mmol $Co(NO_3)_2.6H_2O$.

2.3. Synthesis of Ce-CO and Ce-CS

In order to produce the oxide derivative obtained from Ce-ZIF-67, an appropriate amount of this substance was placed in a porcelain crucible and subjected to a heating process at 350 °C for a

duration of 3 h, with a heating rate of 5 °C per min. The use of this approach resulted in synthesis of Ce-CO.

Furthermore, for the synthesis of the Ce-CS, 250 mg of the synthesized Ce-CO were dispersed in 200 ml of $C_2H_6O_2$ in a 500 ml reaction flask. This mixture was subjected to ultrasonic waves for 15 min using an ultrasonic device. Subsequently, 29.55 mmol of CH_4N_2S were dissolved in 20 ml of $C_2H_6O_2$, and the resulting solution was added to the mixture containing the Ce-CO. The sulfidation reaction proceeded for 4 h under reflux at a temperature of 150 °C. The resultant mixture was washed several times with distilled water and C_2H_6O, then dried in an oven at 60 °C for 8 h.

2.4. Materials characterization

The structure of all the synthesized materials was determined using X-ray diffraction (XRD) with PANalytical (XPert PRo MPD, United Kingdom) equipment utilizing Cu Kα radiation as a source of X-ray. The detection of chemical bonds of materials have been done utilizing a Fourier transform infrared spectrometer (FTIR) by PerkinElmer (Spectrum RX I) instrument (United States). The morphological features of samples were investigated by field emission scanning electron microscope (FE-SEM) TESCAN (MIRA 3 LMU, Czech Republic) equipment and a Zeiss (EM10C-100Kv, Germany) instrument transmission electron microscope (TEM). The elemental chemical characteristics were evaluated using energy dispersive spectroscopy (EDS) by the TESCAN (MIRA 3 LMU) instrument (Czech Republic). The electronic state of ions was analyzed using X-ray photoelectron spectroscopy (XPS) with a Bes Tek instrument (Germany).

## 2.5. Preparation of the working electrode

Initially, NF was divided into pieces of 1×1 cm^2. The pieces were then subjected to ultrasonic waves in an acetone bath for 10 min. Following this, it was immersed in a 2.0 M KOH solution for 4 min, and immediately afterward, it was placed in a 1.0 M HCl solution. Finally, the foam underwent a final washing step under ultrasonic waves in acetone for 5 min to eliminate the oxides and any potential residues from the surface of the NF.

The synthesized catalysts covered the surface of the pretreated NF in the following way for preparing the working electrode: 12 mg of the synthesized material was thoroughly mixed with 2 mg of carbon black. The resulting mixture was then dissolved in a solution obtained by mixing C_5H_9NO and $-(C_2H_2F_2)_n-$ in a 9:1 ratio, and subsequently coated onto the surface of NF. The obtained electrode was placed in an oven at 120 °C for 2 h.

2.6. Electrochemical measurements

Electrochemical analyses were conducted utilizing a RADstat electrochemical workstation (Kian Shar Danesh, Iran) with a standard three-electrode system. The experiments were conducted in a cell containing a 1.0 M KOH solution, which has a pH of 14. The reference electrode was an Ag/AgCl with 3.0 M KCl, while the counter electrode was platinum wire. The covered NFs were employed as the working electrode. The potentials were measured in relation to a reversible hydrogen electrode (RHE), as shown in the following equation:

$$E_{RHE} = E_{Ag/AgCl} + E^0_{Ag/AgCl} + 0.059 \text{ pH} \tag{1}$$
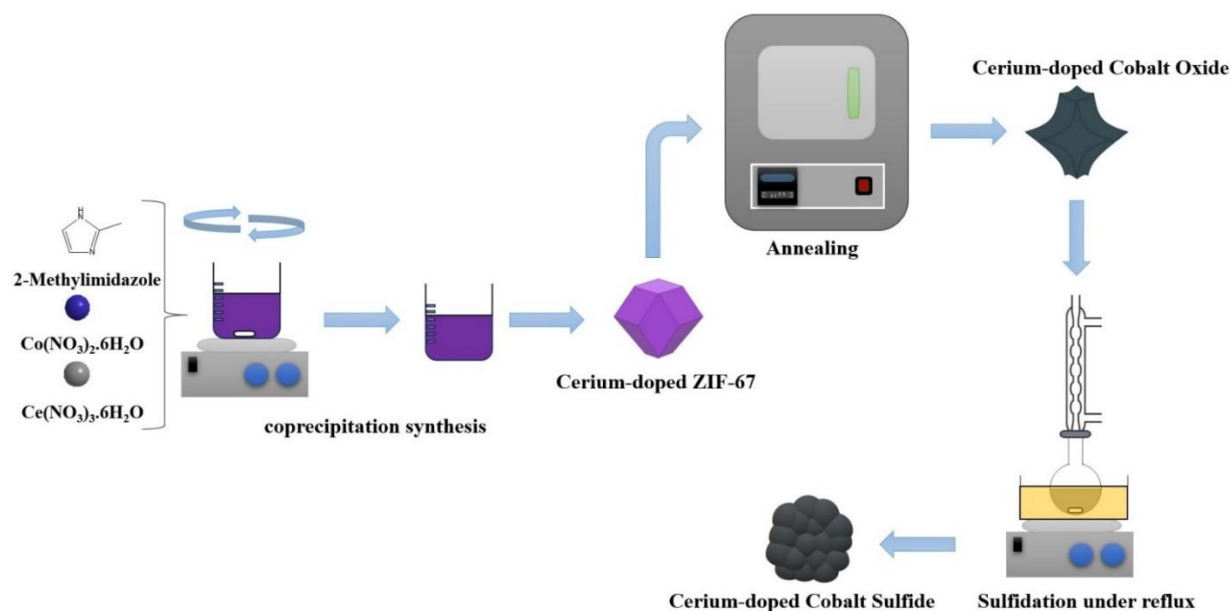
Scheme 1. Schematic of synthesis for Ce-ZIF-67, Ce-CO, and Ce-CS.

3. Results and discussion

3.1. Materials characterization

The synthesized materials were analyzed using XRD to investigate their crystalline structure. Fig. 1a shows that the primary peaks of ZIF-67 occur at precise 2θ angles: 7.32, 10.70, 12.80, 14.79, 16.68, and 18.28. Furthermore, the detected peaks also align with the structural pattern of ZIF-67, demonstrating the synthesis of the material with excellent purity [40]. The specified peaks correspond to the crystalline structures (011), (002), (112), (022), (013), and (222), respectively [41]. The XRD patterns of the bimetallic Ce-ZIF-67 (Fig. 1a) exhibit diffraction peaks at comparable angles, displaying a high intensity. This suggests the production of structures with consistent synthesis and high degree of crystallinity, both in monometallic and bimetallic forms

[42]. It is noteworthy that the addition of cerium to the ZIF-67 structure did not significantly alter its crystalline structure, suggesting that cerium functions as a dopant [43].

The XRD pattern of Ce-CO (Fig. 1a) clearly shows the appearance of new peaks at angles of 19.05, 31.45, 36.95, 44.84, 59.39, and 65.39. These peaks replace those of the Ce-doped ZIF-67, which indicates a successful oxidation procedure. The mentioned diffractions correspond to the crystallographic planes (111), (220), (311), (400), (511), and (440), respectively [44–46]. Moreover, the pattern illustrates the cubic crystal structure of Co_3O_4, which has a lattice constant of 8.076 angstroms and belongs to the space group Fd_3 [47,48].

The XRD analysis of the Ce-CS particles (Fig. 1a) reveals the absence of any detectable peaks associated with cobalt sulfide, indicating the lack of a crystalline phase. This examination reveals that the sulfide particles have a fully amorphous structure [49].

The functional groups of the produced compounds were analyzed using FT-IR analysis at a wavenumber of 400-4000 cm^{-1} (Fig. 1b). The FT-IR peaks seen in both the ZIF-67 and Ce-ZIF-67 structures are similar and consistent with previous investigations [50]. The imidazole ring has been detected in spectral peaks ranging from 600 to 1500 cm^{-1}, which correspond to the stretching and bending vibrations of this ring [51]. The observed peak at 1584 cm^{-1} corresponds to the C=N stretching bond, while aliphatic and aromatic C-H bonds show a stretching vibration peak at 2925 and 3128 cm^{-1} [52,53].

As evidenced by the FT-IR spectrum of Ce-CO structure, some peaks related to the imidazole ring have disappeared due to the oxidation process, and new peaks have emerged in their place, indicating degradation of the organic ligand structure. The peak at 569 cm^{-1} corresponds to the

stretching vibrations of Co-O bonds, while the peak at 667 cm^{-1} is attributed to the vibration of the O-Co-O bond [54,55].

As indicated by the peaks corresponding to the Ce-CS, the peak at 1102 cm^{-1} is attributed to the bending vibration of the S-O group in the sulfonate group of the cobalt sulfide structure. The peak at 670 cm^{-1} corresponds to the stretching vibration of Co-S bonds, albeit with an overlap with the oxide structure [56,57].
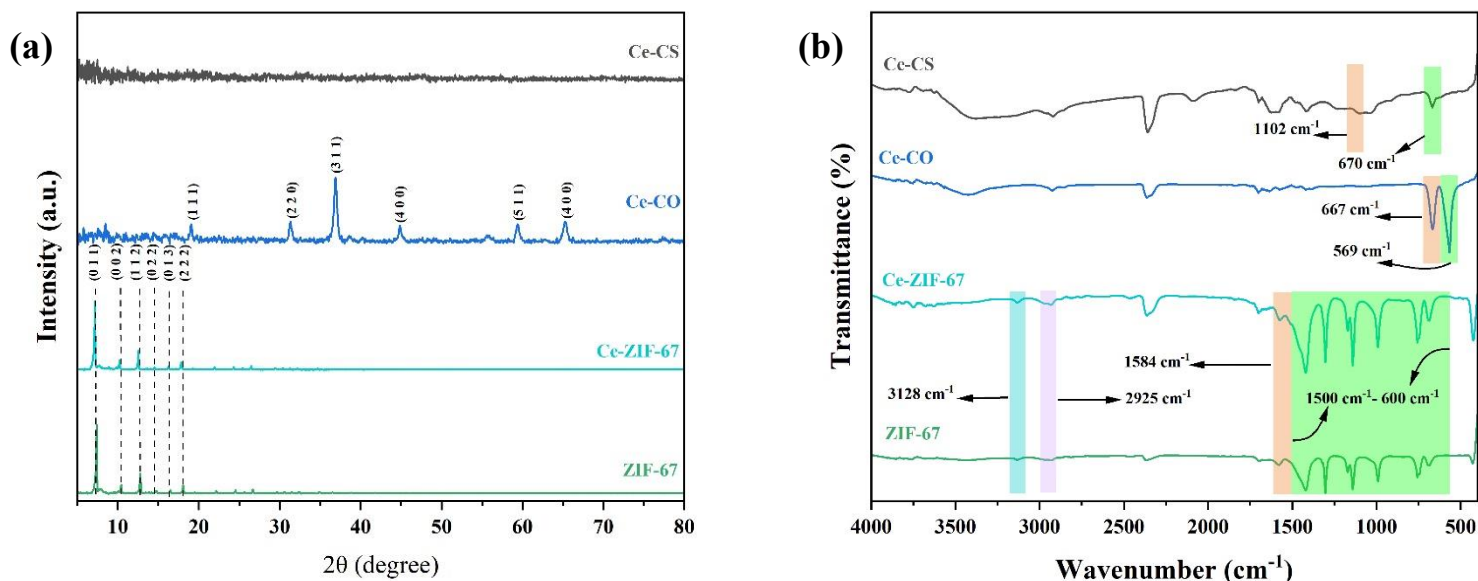

Fig. 1. (a) XRD patterns and (b) FT-IR spectra of ZIF-67, Ce-ZIF-67, Ce-CO, and Ce-CS.

The structure of the synthesized materials was examined using FE-SEM analysis. Fig. 2a illustrates that ZIF-67 possesses a rhombic dodecahedron structure. Fig. 2b depicts the configuration of Ce-ZIF-67, demonstrating that the introduction of cerium into the ZIF-67 structure did not alter its shape, and the required material was synthesized while preserving its polyhedral structure. After the calcination process of Ce-ZIF-67, the resulting material (Ce-CO) maintained its main structure. However, wrinkles were observed on the surface, indicating the oxidation of the target structure,

11

as depicted in Fig. 2c. The structure of Ce-CS is evident in Fig. 2d, which demonstrates the presence of uneven, spherical-shaped nanoparticles after the sulfidation process.

To conduct a more detailed study of the morphology, the structures of Ce-CO and Ce-CS were analyzed using TEM technique. Fig. 2e depicts the formation of rough surface on the Ce-CO structure during the oxidation process, which aligns with the findings from the FE-SEM micrographs. Moreover, Fig. 2f illustrates the existence of nano-spheres in Ce-CS structure.
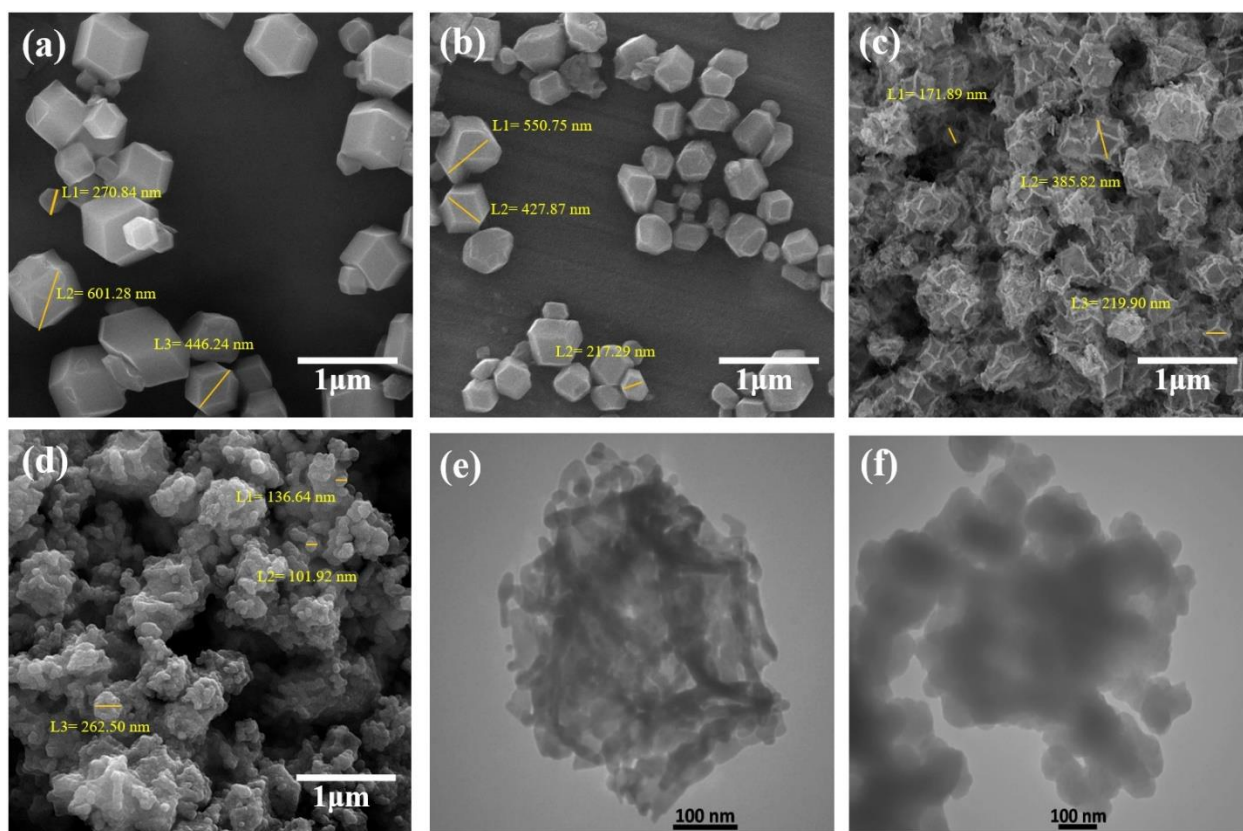
Fig. 2. FESEM micrographs of (a) ZIF-67, (b) Ce-ZIF-67, (c) Ce-CO, and (d) Ce-CS; TEM micrographs of (e) Ce-CO and (f) Ce-CS.

To ascertain the average particle diameter of the synthesized particles, a particle size distribution plot was constructed (Fig. S1, Electronic Supplementary File). The mean particle diameters of ZIF-67, Ce-ZIF-67, Ce-CO, and Ce-CS are 550.51, 350.47, 292.77, and 122.94 nanometers,

respectively. The treatments applied to the ZIF-67 structure have resulted in a noticeable decrease in the average particle size of derived materials.

In Fig. 3a, the EDS analysis of the Ce-CO structure is shown. This analysis indicates the presence of cobalt (Co), oxygen (O), carbon (C), and cerium (Ce) elements in the Ce-CO structure. Fig. 3b clearly demonstrates that the sulfidation process under reflux circumstances led to a substantial incorporation of sulfur (S) into the structure, confirming the effective completion of the sulfidation process. Furthermore, Figs. 4(a-d) and 4(e-i) display the elemental mapping pictures of the Ce-CO and Ce-CS structures, respectively. The results demonstrate an even distribution of all components across the surface of the synthesized materials, signifying their successful synthesis.
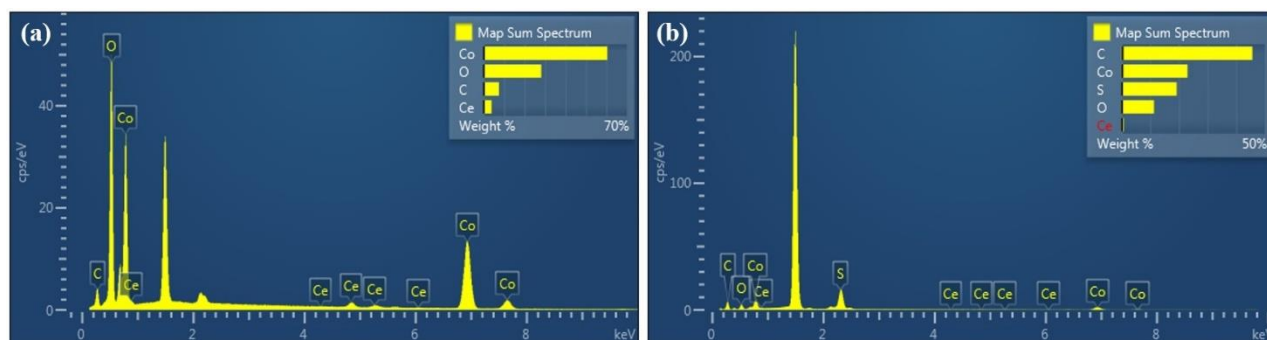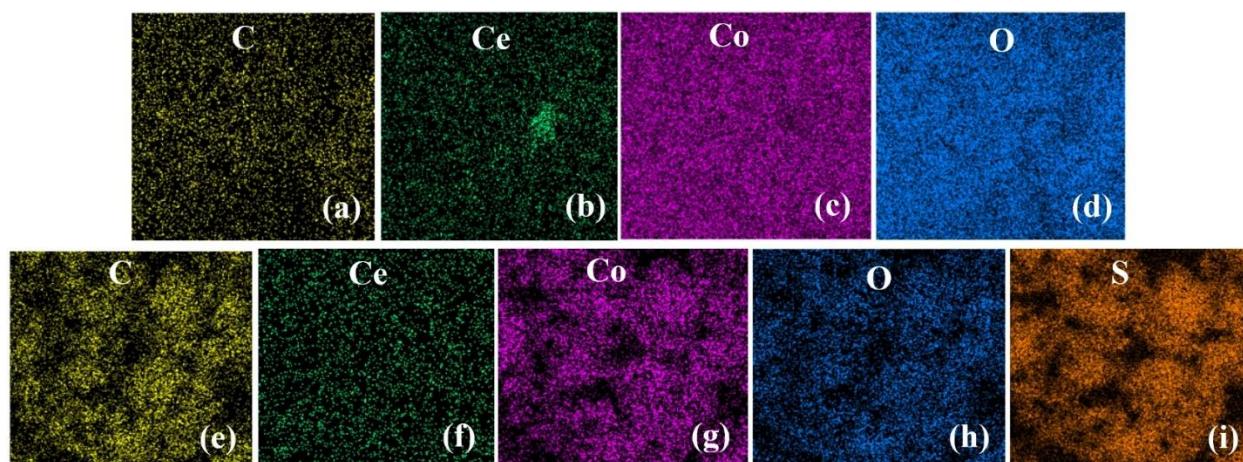

**Fig. 3.** EDS spectrum of (a) Ce-CO and (b) Ce-CS.

13

Fig. 4. Elemental mapping of (a-d) Ce-CO and (e-i) Ce-CS.

XPS analysis employed to further investigate the chemical valence state and composition of Ce-CS. The XPS spectra of the Ce-CS structure, including C 1s, O 1s, S 2p, Co 2p, and Ce 3d, are shown in Fig. 5(a-e). The C 1s peak (Fig. 5a) has been deconvoluted, revealing two peaks positioned at 284.8 eV and 286.4 eV, signifying the presence of the C–C and C–O groups, respectively [58]. The deconvolution of the O 1s peak (Fig. 5b) reveals two distinct components at 532.2 and 534.4 eV, corresponding to surface lattice oxygen (such as metal-oxygen bonds) and adsorbed oxygen (such as hydroxide bonds), respectively [59]. In the XPS spectrum of S 2p (Fig. 5c), peaks at 162.8 and 164.7 eV are S^{2-}, demonstrating the formation of metal sulfides, and the peak position around 168.9 eV can be assigned to the sulfate groups [60]. The Co 2p region (Fig. 5d) displayed doublets at binding energies of 779.7 and 782.2 eV, which corresponded to Co $2p_{3/2}$. Similarly, the peaks observed at 794.6 and 797.4 eV were identified as Co $2p_{1/2}$. Furthermore, two satellite peaks were present at 785.1 and 802.1 eV [61]. The spectrum of Ce 3d is depicted in Fig. 5e, with spin-orbit doublets obtained through deconvolution. The peaks located at 885.6 and 887.8 eV, as well as the peaks observed at 903.3 and 905.6 eV, can be attributed to Ce $3d_{5/2}$ and Ce $3d_{3/2}$, respectively. This provides evidence for the presence of Ce^{3+} and Ce^{4+} in the Ce-CS [62].
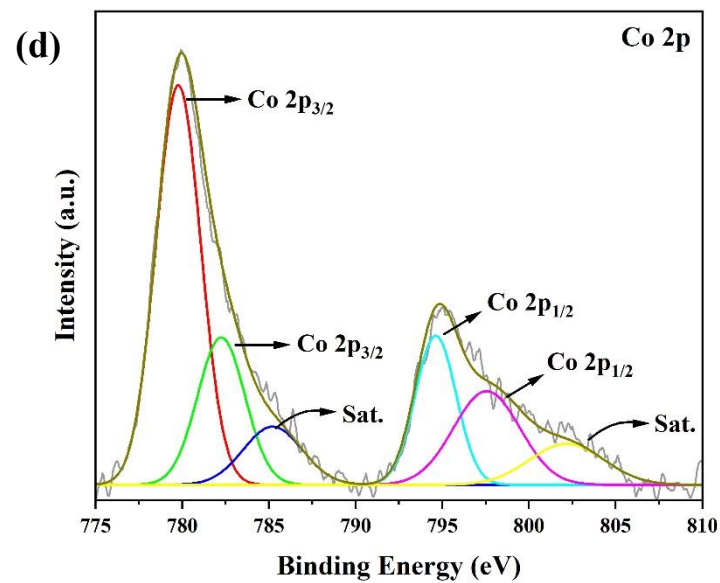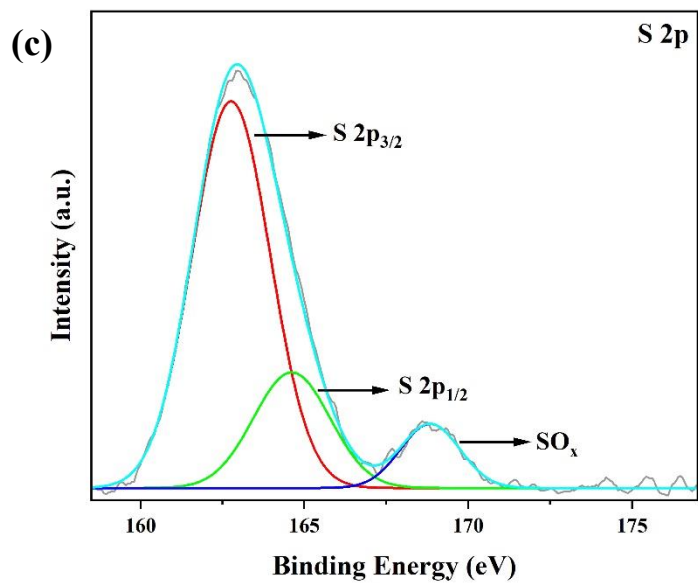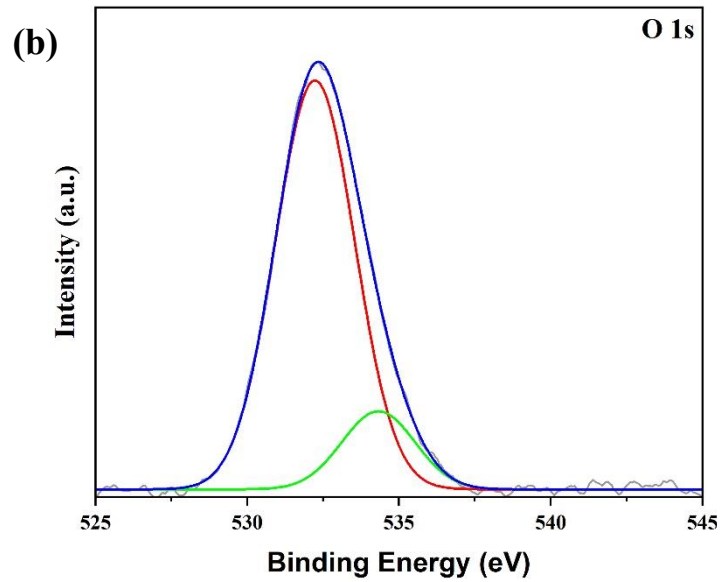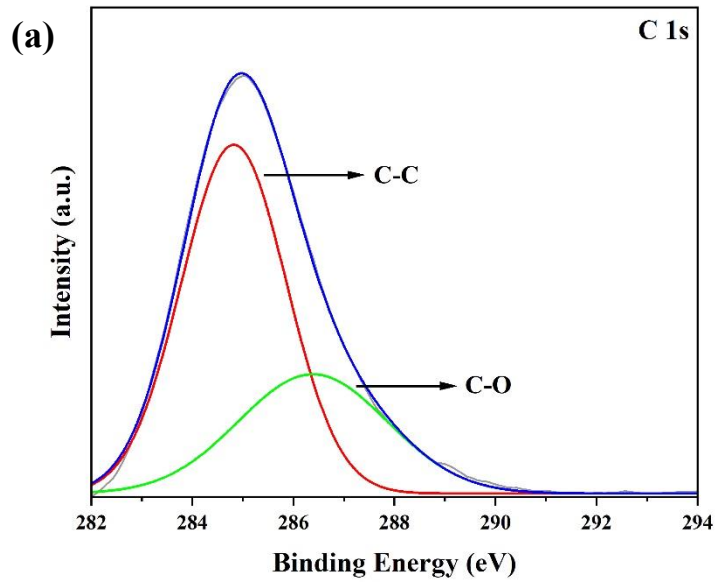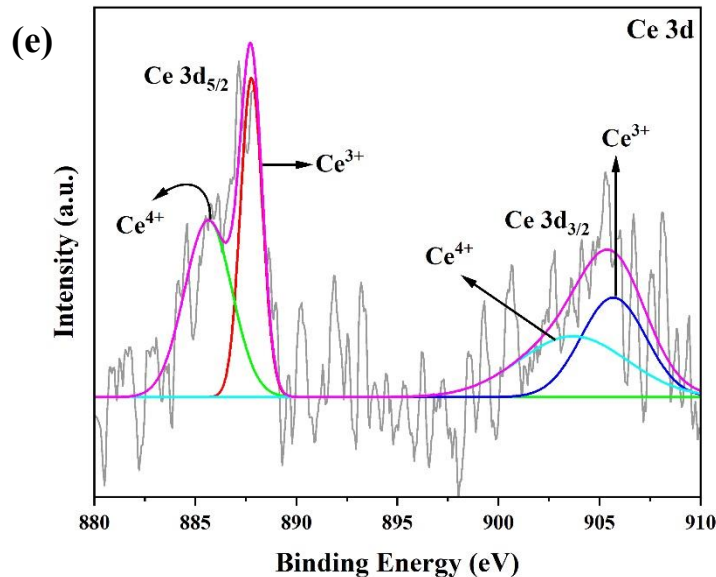
Fig. 5. XPS spectrum of (a) C 1s, (b) O 1s, (c) S 2p, (d) Co 2p, and (e) Ce 3d for Ce-CS sample.

3.2. Electrochemical evaluations

Linear sweep voltammetry (LSV) was conducted to analyze the electrochemical activity of synthesized materials, and all data were gathered at a constant scan rate of 5 mV s^{-1} (Fig. 6a). The voltametric plot demonstrates that the addition of cerium enhances the performance of the ZIF-67 structure. This suggests that the use of bimetallic synthesis in creating the ZIF-67 structure is effective in improving its performance. Additionally, it is noteworthy that the oxidation process positively impacts electron transfer, leading to a noticeable reduction in overpotential [63]. It is evident that the sulfidation process on the Ce-CO structure has a very significant impact on its electrochemical performance in the OER process. The measured overpotentials at a current density of 100 mA cm^{-2} for ZIF-67, Ce-ZIF-67, Ce-CO, and Ce-CS were 446, 415, 352, and 291 mV, respectively. Additionally, these electrodes exhibited overpotentials of 440, 403, 346, and 283 mV

at a current density of 80 mA cm^{-2}. Moreover, the overpotentials at a current density of 60 mA cm^{-2} for these electrodes were recorded as 432, 398, 339, and 260 mV, respectively.

Cobalt and cerium, as transition metals with strong reactivity and cost-effectiveness, are highly suitable for use in the OER process. Through the introduction of cerium into the ZIF-67 structure and utilizing the consequent synergistic effect, the Ce-ZIF-67 structure demonstrated enhanced performance in comparison to ZIF-67. Furthermore, the process of oxidizing the Ce-ZIF-67 structure to create Ce-CO greatly improved the performance of the electrode by increasing its electrochemical active surface area. Additionally, the sulfidation process converted the previously oxidized structure into an amorphous form, which demonstrated substantial performance improvements. The improvement in performance is attributed to the existence of sulfur and the disordered structure, which together facilitate faster electron transfer and considerably reduce the overpotential for the OER [64].

The OER kinetics were investigated using Tafel plots, which depict the relationship between η (overpotential) and log j (j is current density). The Tafel slopes for ZIF-67, Ce-ZIF-67, Ce-CO, and Ce-CS, as shown in Fig. 6b, were determined to be 121.0, 102.0, 86.2, and 67.2 mV decade^{-1}, respectively. These values were obtained by performing linear fits to the Tafel plots. The reduction in the Tafel slope indicates an improvement in reaction kinetics. As the obtained results show, the Ce-CS structure exhibited the lowest Tafel slope, indicating that the sulfidation process of the Ce-CO structure, and the resulting morphological change to amorphous nanospheres, have enhanced the electronic structure, leading to significantly improved reaction kinetics. Furthermore, it is noteworthy that doping the ZIF-67 structure with cerium has positively impacted the reaction kinetics, demonstrating the effectiveness of the doping process on the performance of this structure. The decrease in the Tafel slope observed during oxidation can be attributed to the

formation of regular and stable crystalline networks. Furthermore, it is important to note that the oxidation process eliminates impurities and unstable species, leading to the creation of a more uniform material that is of greater purity [65]. Consequently, the Tafel slope of Ce-CO decreased significantly compared to Ce-ZIF-67. Ultimately, the decreasing trend in the Tafel slope indicates that the synthesis approach used for the final structure was highly effective. Fig. 6c presents the values of overpotentials at different current densities, and values of Tafel slopes for the synthesized materials for facilitating comparison.
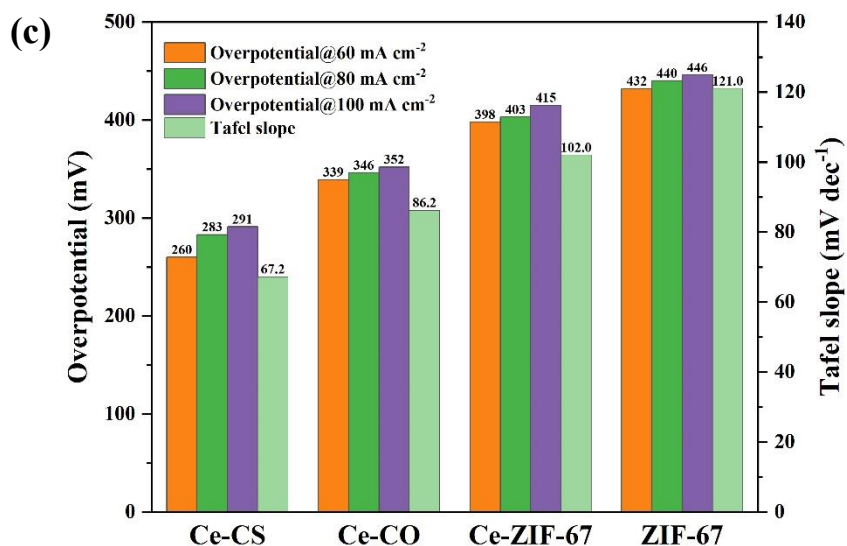
(a)

(b)
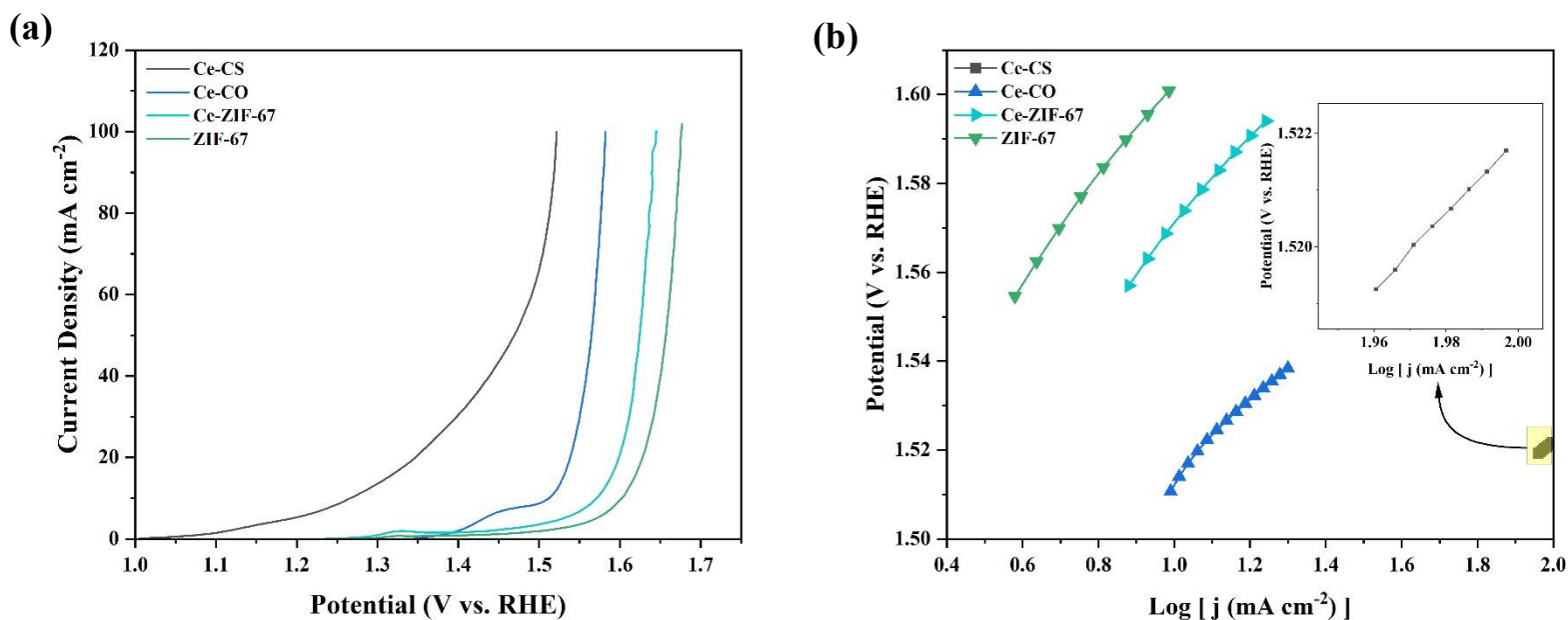
Fig. 6. (a) LSV curves, (b) Tafel diagrams, and (c) measured overpotentials and Tafel slopes of ZIF-67, Ce-ZIF-67, Ce-CO, and Ce-CO.

To determine the electrochemical active surface area (ECSA), it is first necessary to measure the double-layer capacitance (C_{dl}), which can be calculated using the following equation, where Cs represents the specific capacitance.

$$ECSA = \frac{C_{dl}}{C_S} \tag{2}$$

To determine the double-layer capacitance, cyclic voltammetry (CV) tests must be conducted in the non-faradaic region at various scan rates on the synthesized materials. In this study, CV tests were performed at scan rates of 20, 40, 60, 80, and 100 mV s^{-1} on the synthesized materials (Fig. S2, Electronic Supplementary File). The C_{dl} value is obtained by measuring the slope of the plot of the difference between the anodic and cathodic current densities at a fixed voltage versus the scan rate (Δj vs. scan rate). According to Fig. 7, the C_{dl} values obtained for the structures ZIF-67, Ce-ZIF-67, Ce-Co, and Ce-CS are 0.32, 0.53, 1.07, and 1.98 mF cm^{-2}, respectively. A higher C_{dl}

indicates a greater ability of the structure to store charge at the interface, which enhances charge transfer during the process.

Given the direct relationship between ECSA and C_{dl}, it is evident that an increase in C_{dl} leads to an increase in ECSA. It is clear that doping the ZIF-67 structure with cerium has increased the ECSA, and through oxidation and subsequent sulfidation processes, the ECSA has reached its optimal value. The improved ECSA in the final structure suggests the presence of a greater number of active surface sites that are reactive towards chemical reactions. This results in faster electron movement and more efficient interactions between the electrode and electrolyte during the OER process [66].
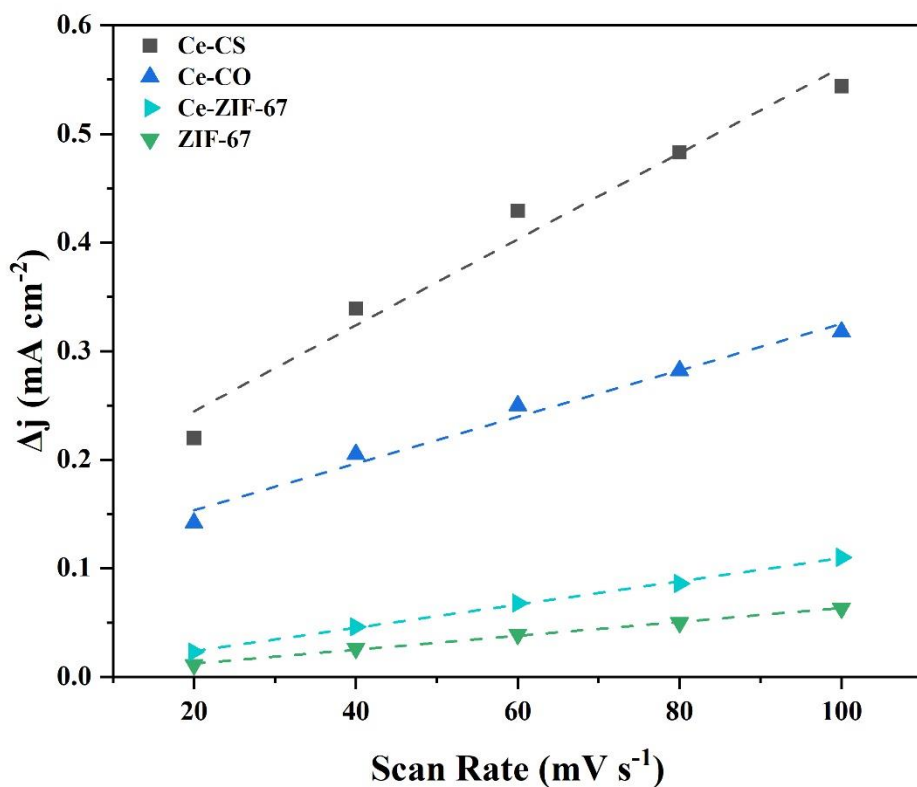
Fig. 7. The electrochemical double layer capacitance of ZIF-67, Ce-ZIF-67, Ce-CO, and Ce-CS

(the dash lines represent the linear regression model applied to the dataset)

A method of electrochemical impedance spectroscopy (EIS) has been used to gain a more comprehensive understanding of the OER kinetics. This measurement was conducted using a constant voltage and a frequency range of $0.1-10^5$ Hz. Fig. 8 illustrates the Nyquist plots of ZIF-67, Ce-ZIF-67, Ce-CO, and Ce-CS. The acquired data can be accurately matched to the equivalent circuit shown in the diagram inset of Fig. 8. The charge transfer resistance (R_{ct}) values for ZIF-67, Ce-ZIF-67, Ce-CO, and Ce-CS are 24.99, 18.64, 11.20, and 3.84 Ω, respectively. The lowest R_{ct} value was shown by Ce-CS, indicating its most rapid electron transfer during the OER process. The initial reduction in electrode resistance is attributed to the bimetallic formation of the ZIF-76 structure. In subsequent steps, by conducting oxidation and sulfidation processes, resulting in an amorphous structure, electron transfer improved [67]. Consequently, the R_{ct} decreased. The R_s values were utilized to offset the ohmic drop resulting from the solution resistance (R_s). The specific R_s values for ZIF-67, Ce-doped ZIF-67, Ce-CO, and Ce-CS electrodes are 4.59, 4.05, 3.9, and 3 Ω, respectively.
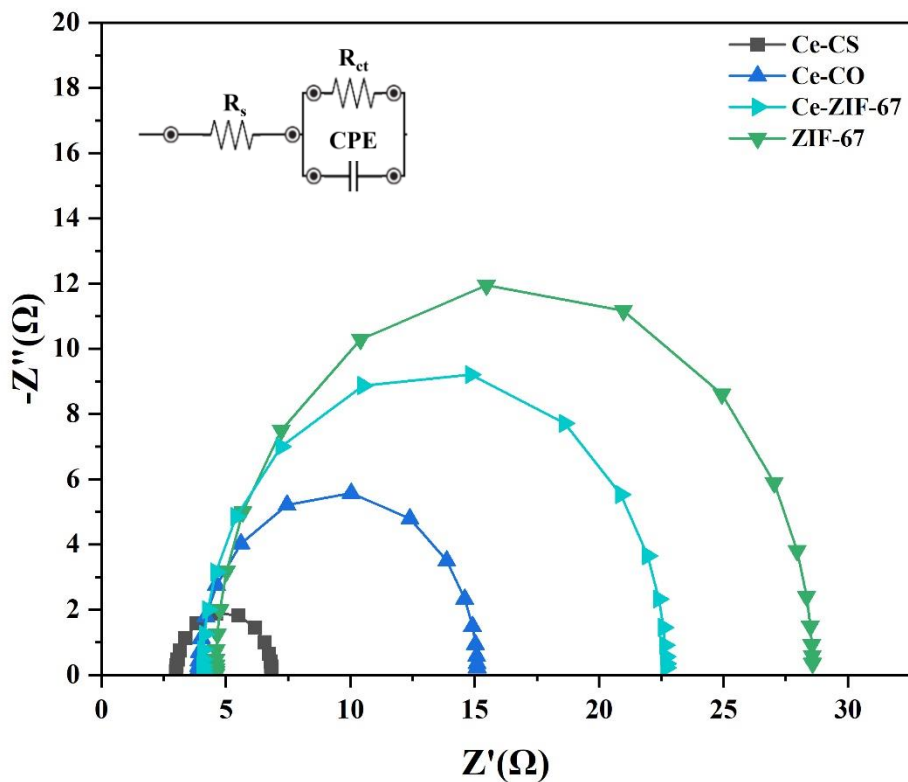
Fig. 8. Nyquist diagrams of ZIF-67, Ce-ZIF-67, Ce-CO, and Ce-CS (shown as a schematic representation of an equivalent circuit)

The stability of the electrode is a vital parameter for evaluating the effectiveness of synthesized electrocatalyst. To assess this, the endurance of Ce-CS was initially examined using chronopotentiometry at a current density of 100 mA cm^{-2}. As shown in Fig. 9, the potential of the electrode stayed nearly constant throughout a stability analysis lasting 10 hours. Additionally, the LSV graph after the stability analysis (after 1000 cycles of CV) matched the first curve of LSV, indicating excellent durability of the synthesized amorphous material. Additionally, the FESEM micrographs before and after chronopotentiometry, as shown in Fig. 9(b-e), indicate that the Ce-CS structure remains largely unchanged after 10 h of operation, with the structure being well-

preserved. The EDS analysis conducted before and after the chronopotentiometry test (Fig. S3(a,b), Electronic Supplementary File) shows that the elemental composition of the Ce-CS structure has not undergone significant changes. The elemental mapping of the Ce-CS electrode structure (Fig. S4(a-j), Electronic Supplementary File) also indicates that the distribution of materials has remained unchanged after chronopotentiometry test, and the elements are uniformly dispersed across the surface. These structural analyses demonstrate that the synthesized structure possesses sufficient stability for use in the OER process.
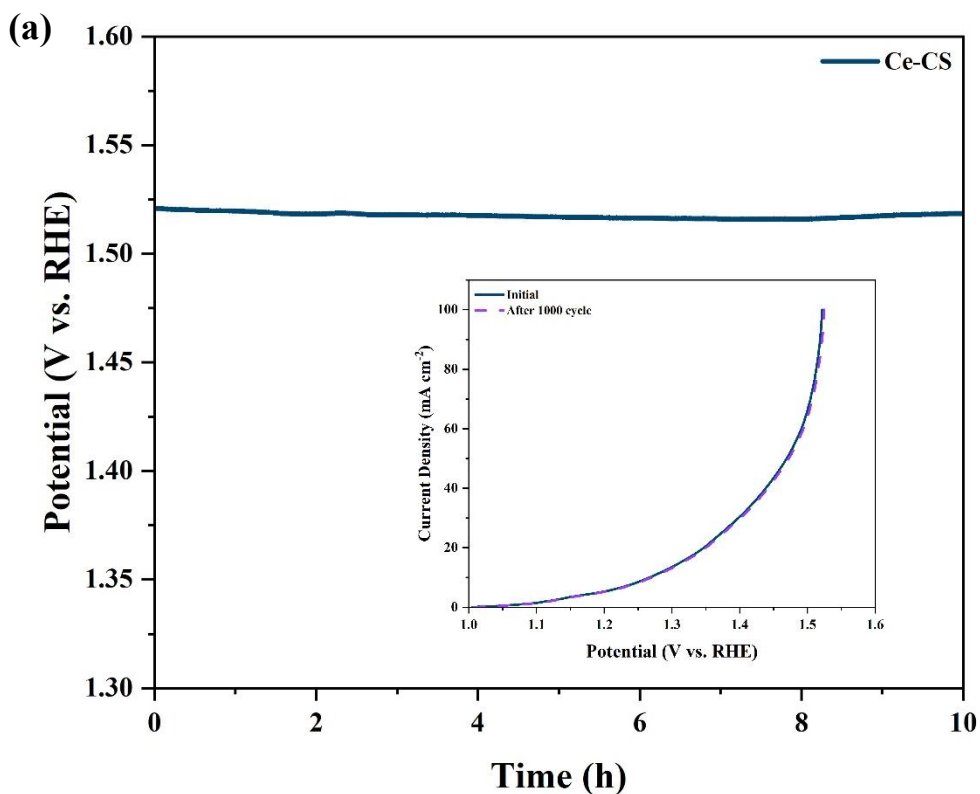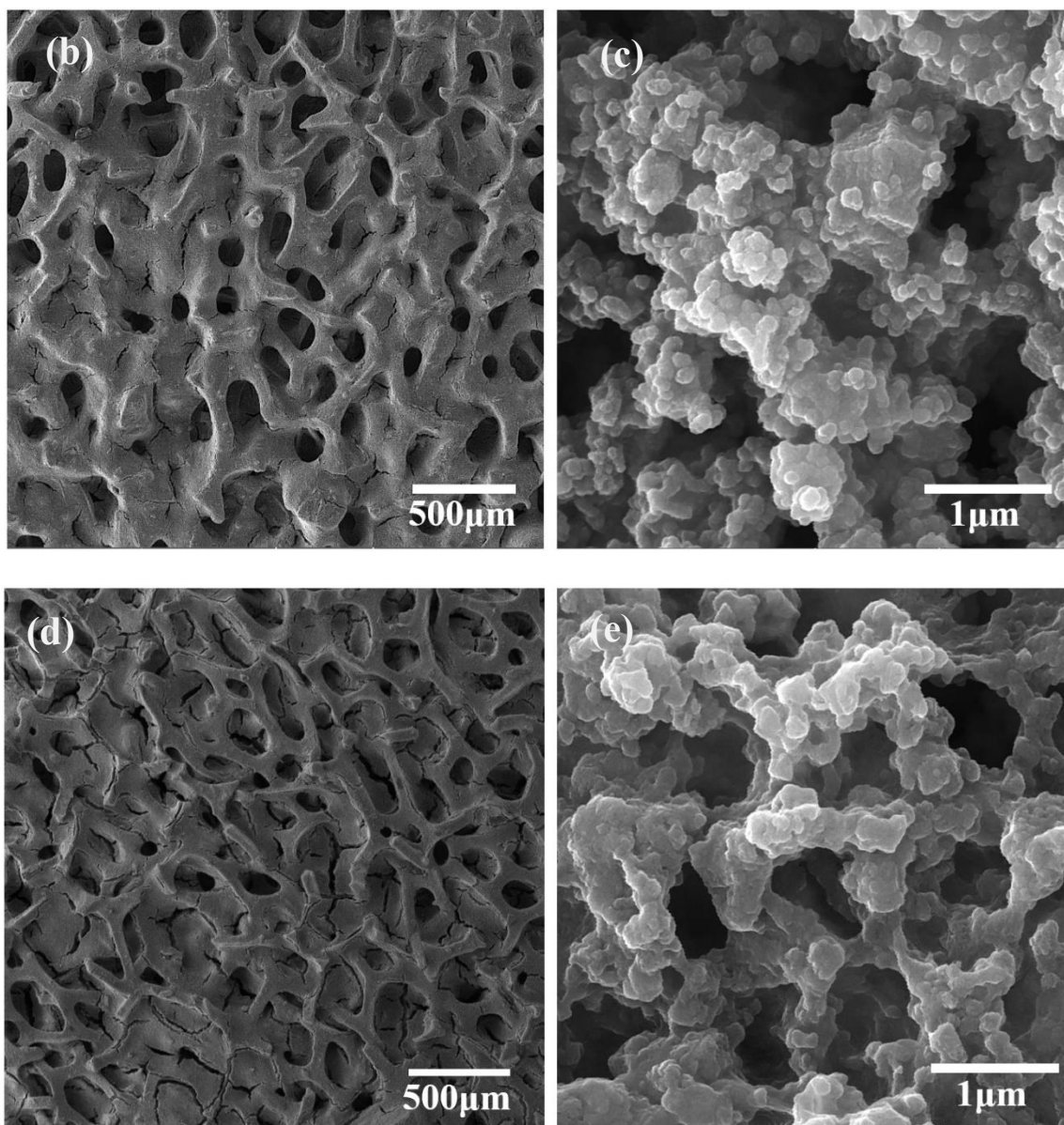
Fig. 9. (a) Chronopotentiometry test of Ce-CS for 10 h (in set is the LSV curves before and after 1000 cycles of CV); FESEM micrographs of Ce-CS (b,c) before it was used and (d,e) after 10 h of use.

In the electrochemical and structural investigations of the materials, it was demonstrated that metal doping of the ZIF-67 structure leads to the formation of unsaturated coordinated sites and atomic defects, which enhance electron transfer during the OER electrocatalytic process. This

improvement is well-aligned with the results of electrochemical analyses, particularly electrochemical impedance spectroscopy (EIS). Moreover, the Ce-ZIF-67 structure effectively provided a robust framework for deriving materials with higher porosity and improved electron transfer capabilities. FESEM analyses reveal that oxidation produces porous ZIF-derived metal oxides with interconnected pores by oxidizing volatile elements (C, N, H) into gaseous products. The oxidation process and the formation of the Ce-CO structure led to changes in the geometrical shape of Ce-ZIF-67, yielding a more porous structure with enhanced performance in all electrochemical analyses. Subsequent sulfidation of the Ce-CO structure, due to the lower electronegativity of the sulfide structures compared to the oxidized ones, resulted in improved performance of the Ce-CS structure over Ce-CO in the electrochemical analyses. Additionally, XRD analysis revealed that the final Ce-CS structure exhibits an amorphous nature. Amorphous materials, characterized by long-range disorder and short-range order extending only over a few atoms, often demonstrate advantages in electrocatalysis compared to their crystalline counterparts. This is due to the presence of more active sites, a broader range of chemical compositions, and higher structural flexibility. These factors contribute to the superior performance of the Ce-CS structure compared to the Ce-CO structure.

Table 1 presents a comparison of the OER performance of Ce-CS with other sulfide-based electrocatalysts. It is evident that the overpotential of Ce-CS at current density of 100 mA cm^{-2} is superior to that of similar materials. This comparison highlights the effectiveness of the synthesis approach used for the Ce-CS catalyst. The combination of cerium doping, metal sulfide incorporation, and the resulting amorphous structure has markedly improved electron transfer, increased the electrochemical active surface area, and consequently enhanced the performance of the Ce-CS structure in the OER process.

Table 1. Comparison of the recent performance of cobalt sulfides in the OER process (at a current density of 100 mA cm^{-2} and under alkaline conditions) has been reported.

Name of electrode	Overpotential (mV)	Reference
NiCoS nanorod	360	[68]
NiCo LDH/NiCoS	308	[69]
Fe- and Ni-codoped CoS_2	295	[70]
FeS_2/CoS_2	302	[71]
Ce-doped FeNi-S_x	294	[72]
Cu@CoS_x/CF	310	[73]
Co-doped Ni_3S_2	340	[74]
CoS_2@CoFe-LDH	358	[75]
Nitrogen-Doped CuO@CuS	392	[76]
Ce-CS	291	This work

4. Conclusion

To summarize, in this work, the effect of cerium doping on ZIF-67 was investigated. Subsequently, the oxidation process yielded the Ce-CO structure, which demonstrated improved performance. Furthermore, a reflux sulfidation process was employed to obtain the amorphous Ce-CS structure, which exhibited superior performance in the OER process. The acquired amorphous structure provided a multitude of active sites for electrochemical processes, resulting in a substantial decrease in ion transfer time and an increase in the surface area of contact between the electrode and electrolyte. This favorable performance is attributed to: 1) the synergistic effect of cerium

doping, which enhances electron transfer, and 2) the amorphous sulfide, which increases the contact surface with active sites. The improved catalyst had a significant overpotential of 291 mV when operating at 100 mA cm^{-2} as a current density. Additionally, it exhibited a small Tafel slope of 67.2 mV decade^{-1}. Additionally, the catalyst exhibited satisfactory durability for extended periods of electrolysis. This work presents an effective approach for creating catalysts that show great overpotential in OER.

References

[1] X. Lu, H. Xu, T. Yang, X. Chen, Z. Cheng, Q. Hou, X. Lin, S. Liu, S. Wei, Z. Wang, Co3+-rich CoFe-PBA encapsulated in ultrathin MoS2 sheath as integrated core-shell architectures for highly efficient OER, J Alloys Compd 942 (2023) 169004. https://doi.org/10.1016/j.jallcom.2023.169004.

[2] C. Kaplan, R.M. Restrepo, T. Schultz, K. Li, V. Nicolosi, N. Koch, M.P. Browne, Effect of the synthesis route and Co Coverage on Co / Ti3C2Tx materials for the oxygen evolution reaction, Electrochim Acta 490 (2024) 144269. https://doi.org/10.1016/j.electacta.2024.144269.

[3] Z. Wu, X.F. Lu, S. Zang, X.W. (David) Lou, Non-Noble-Metal-Based Electrocatalysts toward the Oxygen Evolution Reaction, Adv Funct Mater 30 (2020). https://doi.org/10.1002/adfm.201910274.

[4] Y. Shi, W. Du, W. Zhou, C. Wang, S. Lu, S. Lu, B. Zhang, Unveiling the Promotion of Surface-Adsorbed Chalcogenate on the Electrocatalytic Oxygen Evolution Reaction, Angewandte Chemie International Edition 59 (2020) 22470–22474. https://doi.org/10.1002/anie.202011097.

[5] X. Yu, X. Wang, S. Wu, P. He, F. Qin, Y. Yao, J. Bai, L. Ren, A simple surface phosphating treatment accompanied by the formation of Co-based multiphase heterostructure for efficient oxygen evolution reaction, Surfaces and Interfaces 44 (2024) 103682. https://doi.org/10.1016/j.surfin.2023.103682.

[6] G. Liu, Y. Cheng, M. Qiu, C. Li, A. Bao, Z. Sun, C. Yang, D. Liu, Facilitating interface charge transfer via constructing NiO/NiCo2O4 heterostructure for oxygen evolution reaction under alkaline conditions, J Colloid Interface Sci 643 (2023) 214–222. https://doi.org/10.1016/j.jcis.2023.04.026.

[7] H. Shooshtari Gugtapeh, M. Rezaei, Exploring the mechanisms of catalytic performance enhancement for HER and OER on nickel film by incorporating antimony atoms: DFT study and experimental validation, Surfaces and Interfaces 40 (2023) 103125. https://doi.org/10.1016/j.surfin.2023.103125.

[8]   L. Yao, H. Zhang, M. Humayun, Y. Fu, X. Xu, C. Feng, C. Wang, Constructing nanoporous crystalline/amorphous NiFe2O4/NiO electrocatalyst for high efficiency OER/UOR, J Alloys Compd 936 (2023) 168206. https://doi.org/10.1016/j.jallcom.2022.168206.

[9]   N. Alwadai, S. Manzoor, M. Al Huwayz, M. Abdullah, R.Y. Khosa, S. Aman, A.G. Abid, Z.A. Alrowaili, M.S. Al-Buriahi, H.M.T. Farid, Facile synthesis of transition metal oxide SnO2/MnO2 hierarchical nanostructure: As an efficient electrocatalyst for robust oxygen evolution reaction, Surfaces and Interfaces 36 (2023) 102467. https://doi.org/10.1016/j.surfin.2022.102467.

[10]   Y. Li, X. Yuan, P. Wang, L. Tang, M. He, P. Li, J. Li, Z. Li, Rare earth alloy nanomaterials in electrocatalysis, Journal of Energy Chemistry 83 (2023) 574–594. https://doi.org/10.1016/j.jechem.2023.04.050.

[11]   K.B. Patel, B. Parmar, K. Ravi, R. Patidar, J.C. Chaudhari, D.N. Srivastava, G.R. Bhadu, Metal-organic framework derived core-shell nanoparticles as high performance bifunctional electrocatalysts for HER and OER, Appl Surf Sci 616 (2023) 156499. https://doi.org/10.1016/j.apsusc.2023.156499.

[12]   Y. Li, C. Wang, K. Zhang, J. Li, Z. Wu, C. Wang, Y. Du, Interfacial electronic structure modulation enables PdAg/NiOx an advanced oxygen evolution electrocatalyst, Surfaces and Interfaces 44 (2024) 103640. https://doi.org/10.1016/j.surfin.2023.103640.

[13]   Q. Zhao, Z. Yan, C. Chen, J. Chen, Spinels: Controlled Preparation, Oxygen Reduction/Evolution Reaction Application, and Beyond, Chem Rev 117 (2017) 10121–10211. https://doi.org/10.1021/acs.chemrev.7b00051.

[14]   S. Aman, N. Ahmad, M.B. Tahir, M.M. Alanazi, S.A.M. Abdelmohsen, R.Y. Khosa, H.M.T. Farid, Understanding the spatial configurations of Sm2O3 in NiO interfaces Embedded-Loaded for Electrocatalytic OER process, Surfaces and Interfaces 38 (2023) 102857. https://doi.org/10.1016/j.surfin.2023.102857.

[15]   B. Paul, P. Bhanja, S. Sharma, Y. Yamauchi, Z.A. Alothman, Z.-L. Wang, R. Bal, A. Bhaumik, Morphologically controlled cobalt oxide nanoparticles for efficient oxygen

evolution reaction, J Colloid Interface Sci 582 (2021) 322–332. https://doi.org/10.1016/j.jcis.2020.08.029.

[16] Y. Zhang, H. Guo, M. Song, Z. Qiu, S. Wang, L. Sun, Hierarchical interfaces engineering-driven of the CoS2/MoS2/Ni3S2/NF electrode for high-efficient and stable oxygen evolution and urea oxidation reactions, Appl Surf Sci 617 (2023) 156621. https://doi.org/10.1016/j.apsusc.2023.156621.

[17] A. Mariappan, R.K. Dharman, T.H. Oh, Metal-organic frameworks derived FeS2@CoS2 heterostructure for efficient and stable bifunctional electrocatalytic water splitting, Ceram Int 49 (2023) 29984–29990. https://doi.org/10.1016/j.ceramint.2023.06.255.

[18] M.I.A. Abdel Maksoud, R.A. Fahim, A.E. Shalan, M. Abd Elkodous, S.O. Olojede, A.I. Osman, C. Farrell, A.H. Al-Muhtaseb, A.S. Awed, A.H. Ashour, D.W. Rooney, Advanced materials and technologies for supercapacitors used in energy conversion and storage: a review, Environ Chem Lett 19 (2021) 375–439. https://doi.org/10.1007/s10311-020-01075-w.

[19] Y. Wang, M. Xie, F. Dai, J. Liu, L. Zhang, R. Zhang, Z. Zhang, W. Hu, Iron regulates the interfacial charge distribution of transition metal phosphides for enhanced oxygen evolution reaction, J Colloid Interface Sci 615 (2022) 725–731. https://doi.org/10.1016/j.jcis.2022.02.009.

[20] M. Beshtar, A. Larimi, A.A. Asgharinezhad, F. Khorasheh, Ultra-deep Photocatalytic Oxidative Desulfurization of Model Fuel Using Ti-UiO-66(Zr) Metal–Organic Framework, Catal Letters (2023). https://doi.org/10.1007/s10562-023-04506-9.

[21] X. Chen, Y. Li, X. Zhao, Screening of transition metal-based MOF as highly efficient bifunctional electrocatalysts for oxygen reduction and oxygen evolution, Surfaces and Interfaces 38 (2023) 102821. https://doi.org/10.1016/j.surfin.2023.102821.

[22] B. Yang, Y. Du, M. Shao, D. Bin, Q. Zhao, Y. Xu, B. Liu, H. Lu, MOF-derived RuCoP nanoparticles-embedded nitrogen-doped polyhedron carbon composite for enhanced water splitting in alkaline media, J Colloid Interface Sci 616 (2022) 803–812. https://doi.org/10.1016/j.jcis.2022.02.119.

[23] R. Dargahi, H. Ebrahimzadeh, A.A. Asgharinezhad, A. Hashemzadeh, M.M. Amini, Dispersive magnetic solid-phase extraction of phthalate esters from water samples and human plasma based on a nanosorbent composed of MIL-101(Cr) metal–organic framework and magnetite nanoparticles before their determination by GC–MS, J Sep Sci 41 (2018) 948–957. https://doi.org/10.1002/jssc.201700700.

[24] P. Bhanja, B. Mohanty, B. Paul, A. Bhaumik, B.K. Jena, S. Basu, Novel microporous organic-inorganic hybrid metal phosphonates as electrocatalysts towards water oxidation reaction, Electrochim Acta 416 (2022) 140277. https://doi.org/10.1016/j.electacta.2022.140277.

[25] H. Wang, C. Sun, E. Zhu, C. Shi, J. Yu, M. Xu, Core-shell MOF-derived Fe3C-Co-NC as high-performance ORR/OER bifunctional catalyst, J Alloys Compd 948 (2023) 169728. https://doi.org/10.1016/j.jallcom.2023.169728.

[26] T. Lastovina, A. Budnyk, Y. Pimonova, A. Bugaev, V. Dmitriev, Thermally-induced arrangement of cobalt and iron in the ZIF-derived Fe,Co,Zn-N/C catalysts for the oxygen reduction reaction, Int J Hydrogen Energy 44 (2019) 23010–23022. https://doi.org/10.1016/j.ijhydene.2019.07.022.

[27] L. Zhou, S. Lu, S. Guo, Recent progress on precious metal single atom materials for water splitting catalysis, SusMat 1 (2021) 194–210. https://doi.org/10.1002/sus2.15.

[28] T. Tang, W. Jiang, S. Niu, N. Liu, H. Luo, Q. Zhang, W. Wen, Y. Chen, L. Huang, F. Gao, J. Hu, Kinetically Controlled Coprecipitation for General Fast Synthesis of Sandwiched Metal Hydroxide Nanosheets/Graphene Composites toward Efficient Water Splitting, Adv Funct Mater 28 (2018). https://doi.org/10.1002/adfm.201704594.

[29] B. Dong, K.-L. Yan, Z.-Z. Liu, J.-Q. Chi, W.-K. Gao, J.-H. Lin, F.-N. Dai, Y.-M. Chai, C.-G. Liu, Urchin-Like Nanorods of Binary NiCoS Supported on Nickel Foam for Electrocatalytic Overall Water Splitting, J Electrochem Soc 165 (2018) H102–H108. https://doi.org/10.1149/2.0351803jes.

[30] Y. Lu, L. Tang, P. Wang, M. He, C. Yang, Z. Li, Rare Earth-Based Alloy Nanostructure for Hydrogen Evolution Reaction, ACS Catal 13 (2023) 13804–13815. https://doi.org/10.1021/acscatal.3c03350.

[31] X. Guo, M. Li, L. Qiu, F. Tian, L. He, S. Geng, Y. Liu, Y. Song, W. Yang, Y. Yu, Engineering electron redistribution of bimetallic phosphates with CeO2 enables high-performance overall water splitting, Chemical Engineering Journal 453 (2023) 139796. https://doi.org/10.1016/j.cej.2022.139796.

[32] X. Long, H. Lin, D. Zhou, Y. An, S. Yang, Enhancing Full Water-Splitting Performance of Transition Metal Bifunctional Electrocatalysts in Alkaline Solutions by Tailoring CeO $_2$ – Transition Metal Oxides–Ni Nanointerfaces, ACS Energy Lett 3 (2018) 290–296. https://doi.org/10.1021/acsenergylett.7b01130.

[33] C. Li, P. Wang, M. He, X. Yuan, Z. Fang, Z. Li, Rare earth-based nanomaterials in electrocatalysis, Coord Chem Rev 489 (2023) 215204. https://doi.org/10.1016/j.ccr.2023.215204.

[34] M. Li, X. Pan, M. Jiang, Y. Zhang, Y. Tang, G. Fu, Interface engineering of oxygen-vacancy-rich CoP/CeO2 heterostructure boosts oxygen evolution reaction, Chemical Engineering Journal 395 (2020) 125160. https://doi.org/10.1016/j.cej.2020.125160.

[35] W. Li, L. Zhao, C. Wang, X. Lu, W. Chen, Interface Engineering of Heterogeneous CeO $_2$ – CoO Nanofibers with Rich Oxygen Vacancies for Enhanced Electrocatalytic Oxygen Evolution Performance, ACS Appl Mater Interfaces 13 (2021) 46998–47009. https://doi.org/10.1021/acsami.1c11101.

[36] Z. Guo, L. Liu, J. Wang, Y. Cao, J. Tu, X. Zhang, L. Ding, Recent progress in CoP-based materials for electrochemical water splitting, Int J Hydrogen Energy 46 (2021) 34194–34215. https://doi.org/10.1016/j.ijhydene.2021.07.236.

[37] S. Anantharaj, S. Noda, Amorphous Catalysts and Electrochemical Water Splitting: An Untold Story of Harmony, Small 16 (2020). https://doi.org/10.1002/smll.201905779.

[38] S. Yang, F. Jiao, Y. Gong, Electrochemical crystalline/amorphous Ni(OH)S@CoFe-LDH/NF for efficient oxygen evolution reaction, Sep Purif Technol 331 (2024) 125716. https://doi.org/10.1016/j.seppur.2023.125716.

[39] H. Huang, A. Cho, S. Kim, H. Jun, A. Lee, J.W. Han, J. Lee, Structural Design of Amorphous CoMoP $_x$ with Abundant Active Sites and Synergistic Catalysis Effect for Effective Water Splitting, Adv Funct Mater 30 (2020). https://doi.org/10.1002/adfm.202003889.

[40] X. He, X. Yi, F. Yin, B. Chen, G. Li, H. Yin, An iodine-treated metal-organic framework with enhanced catalytic activity for oxygen reduction reaction in alkaline electrolyte, Electrochim Acta 337 (2020) 135825. https://doi.org/10.1016/j.electacta.2020.135825.

[41] H. Gao, Y. Liu, Y. Ma, E. Meng, Y. Zhang, Synthesis of N-doped Co@C/CNT materials based on ZIF-67 and their electrocatalytic performance for oxygen reduction, Ionics (Kiel) 27 (2021) 2561–2569. https://doi.org/10.1007/s11581-021-04031-y.

[42] Z. Wang, Z. Wang, J. Wang, H. Shi, C. Wang, Y. Fan, Z. Bai, C. Zhu, X. Yan, Ni, Zn Co-doping ZIF-67-derived electrocatalyst based on CNT film for efficient overall water splitting, Int J Hydrogen Energy 48 (2023) 29189–29197. https://doi.org/10.1016/j.ijhydene.2023.04.082.

[43] L. Zhao, C. Gong, X. Chen, X. He, H. Chen, X. Du, D. Wang, W. Fang, H. Zhang, W. Li, ZIF-67 derived Mo-CoS2 nanoparticles embedded in hierarchically porous carbon hollow sphere for efficient overall water splitting, Appl Surf Sci 623 (2023) 157030. https://doi.org/10.1016/j.apsusc.2023.157030.

[44] J. Shen, J. Gao, L. Ji, X. Chen, C. Wu, Three-dimensional interlinked Co3O4-CNTs hybrids as novel oxygen electrocatalyst, Appl Surf Sci 497 (2019) 143818. https://doi.org/10.1016/j.apsusc.2019.143818.

[45] L. Qian, W. Dong, H. Li, X. Song, Y. Ding, Fe-doped NiCo2S4 catalyst derived from ZIF – 67 towards efficient hydrogen evolution reaction, Int J Hydrogen Energy 47 (2022) 8820–8828. https://doi.org/10.1016/j.ijhydene.2021.12.256.

[46] A.A. Asgharinezhad, H. Ebrahimzadeh, Magnetic porous carbon nanocomposite derived from cobalt based-metal-organic framework for extraction and determination of homo and hetero-polycyclic aromatic hydrocarbons, Talanta 233 (2021) 122526. https://doi.org/10.1016/j.talanta.2021.122526.

[47] S. Ambika, S. Gopinath, K. Saravanan, K. Sivakumar, C. Ragupathi, T.A. Sukantha, Structural, morphological and optical properties and solar cell applications of thioglycolic routed nano cobalt oxide material, Energy Reports 5 (2019) 305–309. https://doi.org/10.1016/j.egyr.2019.02.005.

[48] A.A. Asgharinezhad, H. Ebrahimzadeh, A novel polymer coated magnetic porous carbon nanocomposite derived from a metal-organic framework for multi-target environmental pollutants preconcentration, J Chromatogr A 1634 (2020) 461664. https://doi.org/10.1016/j.chroma.2020.461664.

[49] Z. Jiang, W. Lu, Z. Li, K.H. Ho, X. Li, X. Jiao, D. Chen, Synthesis of amorphous cobalt sulfide polyhedral nanocages for high performance supercapacitors, J. Mater. Chem. A 2 (2014) 8603–8606. https://doi.org/10.1039/C3TA14430E.

[50] A. Khan, M. Ali, A. Ilyas, P. Naik, I.F.J. Vankelecom, M.A. Gilani, M.R. Bilad, Z. Sajjad, A.L. Khan, ZIF-67 filled PDMS mixed matrix membranes for recovery of ethanol via pervaporation, Sep Purif Technol 206 (2018) 50–58. https://doi.org/10.1016/j.seppur.2018.05.055.

[51] G. Pang, M. Ji, Z. Li, Z. Yang, X. Qiu, Y. Zhao, Electrospinning of ZIF-67 Derived Co-C-N Composite Efficiently Activating Peroxymonosulfate to Degrade Dimethyl Phthalate, Water (Basel) 14 (2022) 2248. https://doi.org/10.3390/w14142248.

[52] Y. Zolfaghari, M. Ghorbani, M.S. Lashkenari, Electrochemical study on zeolitic imidazolate framework -67 modified MnFe2O4/CNT nanocomposite for supercapacitor electrode, Electrochim Acta 380 (2021) 138234. https://doi.org/10.1016/j.electacta.2021.138234.

[53] S. Rafiei, S. Tangestaninejad, P. Horcajada, M. Moghadam, V. Mirkhani, I. Mohammadpoor-Baltork, R. Kardanpour, F. Zadehahmadi, Efficient biodiesel production

using a lipase@ZIF-67 nanobioreactor, Chemical Engineering Journal 334 (2018) 1233–1241. https://doi.org/10.1016/j.cej.2017.10.094.

[54]   N. Liu, P. Tao, C. Jing, W. Huang, X. Zhang, M. Wu, J. Lei, L. Tang, A facile fabrication of nanoflower-like Co3O4 catalysts derived from ZIF-67 and their catalytic performance for CO oxidation, J Mater Sci 53 (2018) 15051–15063. https://doi.org/10.1007/s10853-018-2696-3.

[55]   R.S. Reena, A. Aslinjensipriya, M. Jose, S.J. Das, Investigation on structural, optical and electrical nature of pure and Cr-incorporated cobalt oxide nanoparticles prepared via co-precipitation method for photocatalytic activity of methylene blue dye, Journal of Materials Science: Materials in Electronics 31 (2020) 22057–22074. https://doi.org/10.1007/s10854-020-04708-6.

[56]   S. Nandhini, G. Muralidharan, The binder-free mesoporous CoNi2S4 electrode for high-performance symmetric and asymmetric supercapacitor devices, J Mater Sci 57 (2022) 5933–5953. https://doi.org/10.1007/s10853-022-06987-2.

[57]   R. Ramachandran, M. Saranya, C. Santhosh, V. Velmurugan, B.P.C. Raghupathy, S.K. Jeong, A.N. Grace, Co $_9$ S $_8$ nanoflakes on graphene (Co $_9$ S $_8$ /G) nanocomposites for high performance supercapacitors, RSC Adv. 4 (2014) 21151–21162. https://doi.org/10.1039/C4RA01515K.

[58]   Y. Li, Y. Fu, W. Liu, Y. Song, L. Wang, Hollow Co-Co3O4@CNTs derived from ZIF-67 for lithium ion batteries, J Alloys Compd 784 (2019) 439–446. https://doi.org/10.1016/j.jallcom.2019.01.085.

[59]   A.G. Dymerska, B. Środa, B. Zielińska, E. Mijowska, In situ insight into the low-temperature promotion of ZIF-67 in electrocatalytic oxygen evolution reaction, Mater Des 226 (2023) 111637. https://doi.org/10.1016/j.matdes.2023.111637.

[60]   G. Li, P. Wang, C. Li, Z. Fang, M. He, W. Wang, X. Yuan, H. Li, P. Li, Z. Li, Cobalt–nickel layered double hydroxide on hollow Co $_3$ S $_4$ /CuS derived from ZIF-67 for efficient overall water splitting, Mater Res Lett 10 (2022) 744–753. https://doi.org/10.1080/21663831.2022.2095235.

[61] T. Chen, Y. Fu, W. Liao, Y. Zhang, M. Qian, H. Dai, X. Tong, Q. Yang, Fabrication of Cerium-Doped CoMoP/MoP@C Heterogeneous Nanorods with High Performance for Overall Water Splitting, Energy & Fuels 35 (2021) 14169–14176. https://doi.org/10.1021/acs.energyfuels.1c01971.

[62] Z. Feng, J. Pu, M. Liu, W. Zhang, X. Zhang, L. Cui, J. Liu, Facile construction of hierarchical Co3S4/CeO2 heterogeneous nanorod array on cobalt foam for electrocatalytic overall water splitting, J Colloid Interface Sci 613 (2022) 806–813. https://doi.org/10.1016/j.jcis.2022.01.081.

[63] J.S. Kim, B. Kim, H. Kim, K. Kang, Recent Progress on Multimetal Oxide Catalysts for the Oxygen Evolution Reaction, Adv Energy Mater 8 (2018). https://doi.org/10.1002/aenm.201702774.

[64] T. Li, K. Jiang, Y. Li, H. Luo, Z. Wang, Y.-Q. Liu, Crystalline nickel sulfide integrated with amorphous cobalt sulfide as an efficient bifunctional electrocatalyst for water splitting, Int J Hydrogen Energy 48 (2023) 7337–7345. https://doi.org/10.1016/j.ijhydene.2022.11.107.

[65] B. Purnama, A.T. Wijayanta, Suharyana, Effect of calcination temperature on structural and magnetic properties in cobalt ferrite nano particles, J King Saud Univ Sci 31 (2019) 956–960. https://doi.org/10.1016/j.jksus.2018.07.019.

[66] S. Sun, X. Zhou, B. Cong, W. Hong, G. Chen, Tailoring the d-Band Centers Endows (Ni $_x$ Fe $_{1-x}$) $_2$ P Nanosheets with Efficient Oxygen Evolution Catalysis, ACS Catal 10 (2020) 9086–9097. https://doi.org/10.1021/acscatal.0c01273.

[67] H. Zhou, M. Zheng, H. Pang, Synthesis of hollow amorphous cobalt phosphide-cobalt oxide composite with interconnected pores for oxygen evolution reaction, Chemical Engineering Journal 416 (2021) 127884. https://doi.org/10.1016/j.cej.2020.127884.

[68] B. Dong, K.-L. Yan, Z.-Z. Liu, J.-Q. Chi, W.-K. Gao, J.-H. Lin, F.-N. Dai, Y.-M. Chai, C.-G. Liu, Urchin-Like Nanorods of Binary NiCoS Supported on Nickel Foam for Electrocatalytic Overall Water Splitting, J Electrochem Soc 165 (2018) H102–H108. https://doi.org/10.1149/2.0351803jes.

[69] J. Li, L. Wang, H. He, Y. Chen, Z. Gao, N. Ma, B. Wang, L. Zheng, R. Li, Y. Wei, J. Xu, Y. Xu, B. Cheng, Z. Yin, D. Ma, Interface construction of NiCo LDH/NiCoS based on the 2D ultrathin nanosheet towards oxygen evolution reaction, Nano Res 15 (2022) 4986–4995. https://doi.org/10.1007/s12274-022-4144-6.

[70] W. Peng, A. Deshmukh, N. Chen, Z. Lv, S. Zhao, J. Li, B. Yan, X. Gao, L. Shang, Y. Gong, L. Wu, M. Chen, T. Zhang, H. Gou, Deciphering the Dynamic Structure Evolution of Fe- and Ni-Codoped CoS_2 for Enhanced Water Oxidation, ACS Catal 12 (2022) 3743–3751. https://doi.org/10.1021/acscatal.2c00328.

[71] Y. Li, J. Yin, L. An, M. Lu, K. Sun, Y. Zhao, D. Gao, F. Cheng, P. Xi, FeS_2/CoS_2 Interface Nanosheets as Efficient Bifunctional Electrocatalyst for Overall Water Splitting, Small 14 (2018). https://doi.org/10.1002/smll.201801070.

[72] W. Xu, G. Wang, Q. Liu, X. Sun, X. Ma, Z. Cheng, J. Wu, M. Shi, J. Zhu, Y. Qi, Doping vacancy synergy engineering: Ce-doped FeNi-Sx micro-succulent ameliorating electrocatalytic oxygen evolution performance, Electrochim Acta 431 (2022) 141133. https://doi.org/10.1016/j.electacta.2022.141133.

[73] Y. Liu, Q. Li, R. Si, G. Li, W. Li, D. Liu, D. Wang, L. Sun, Y. Zhang, X. Zou, Coupling Sub-Nanometric Copper Clusters with Quasi-Amorphous Cobalt Sulfide Yields Efficient and Robust Electrocatalysts for Water Splitting Reaction, Advanced Materials 29 (2017). https://doi.org/10.1002/adma.201606200.

[74] M. Yue, X. He, S. Sun, Y. Sun, M.S. Hamdy, M. Benaissa, A.A.M. Salih, J. Liu, X. Sun, Co-doped Ni3S2 nanosheet array: A high-efficiency electrocatalyst for alkaline seawater oxidation, Nano Res 17 (2024) 1050–1055. https://doi.org/10.1007/s12274-023-6002-6.

[75] G. Afshan, S. Karim, Y.P. Kharwar, T. Aziz, S. Saha, S. Roy, A. Dutta, Green H_2 Generation from Seawater Deploying a Bifunctional Hetero-Interfaced CoS_2-CoFe-Layered Double Hydroxide in an Electrolyzer, Small (2024). https://doi.org/10.1002/smll.202406431.

[76] A.T.A. Ahmed, A.S. Ansari, V.G. Sree, A. Jana, A. Meena, S. Sekar, S. Cho, H. Kim, H. Im, Nitrogen-Doped CuO@CuS Core–Shell Structure for Highly Efficient Catalytic OER Application, Nanomaterials 13 (2023) 3160. https://doi.org/10.3390/nano13243160.